



Short communication

Analysis of ash emissions from the 2020 Nishinoshima eruption using ASTER thermal infrared orbital data

Daniel B. Williams*, Michael S. Ramsey

Department of Geology and Environmental Science, University of Pittsburgh, 4107 O'Hara Street, Pittsburgh, PA 15260, USA

ARTICLE INFO

Article history:

Received 11 February 2021

Received in revised form 28 July 2021

Accepted 6 November 2021

Available online 12 November 2021

Keywords:

Thermal infrared

Emissivity

ASTER

Volcanic ash

Nishinoshima

ABSTRACT

The 2020 eruption of the Nishinoshima volcano, Japan, emplaced new lava flows as well as numerous ash plumes from explosive eruptions. Several of these plumes were imaged by the Advanced Spaceborne Thermal Emission and reflection Radiometer (ASTER) as part of the Urgent Request Protocol (URP) during July 2020. Linear spectral deconvolution was used to model ASTER thermal infrared (TIR) data using the ASTER Volcanic Ash Library (AVAL), a spectral library containing volcanic ash compositional and particle size range end members. The airborne ash plume best matched the andesite library end member suites having a significant fine (<25 μm) fraction proximal to the vent, however particles >63 μm were also detected downwind, and distally around the cloud edges, assumed due to sampling of lower levels of the plume containing these larger particles even as the optical depth remains high. These results demonstrate that both composition and particle size variations within a plume can be estimated from the high spatial and spectral resolution ASTER TIR data using this approach, provided that representative spectral end members are present in AVAL and where the plume remains opaque to upwelling radiance.

© 2021 The Authors. Published by Elsevier B.V. This is an open access article under the CC BY license (<http://creativecommons.org/licenses/by/4.0/>).

1. Introduction

Nishinoshima, a volcanic island located in the western Pacific Ocean, is part of a line of volcanoes and submarine seamounts formed from the subduction of the Pacific plate underneath the Philippine Plate along the Izu-Bonin Trench (Špičák et al., 2009; Fig. 1). Volcanic activity originally began at Nishinoshima in 1973–74, resulting in the formation of a cinder cone and lava flow fields (Osaka et al., 1974), however most of this island was later eroded away (Tamura et al., 2019). A new eruption began at Nishinoshima in November 2013, producing lava effusion, strombolian-style explosive activity, and a new volcanic edifice, which lasted until 2015 (Maeno et al., 2016). In 2017, activity began once again, typified by small scale explosions and lava effusion that reached the coast (Tamura et al., 2019). Renewed activity was reported in 2018, and from December 2019 through 2020, Nishinoshima produced new lava flows, as well as increasingly large ash and gas plumes, which were erupted from 2.4 to 8.3 km high into the atmosphere as late as 18 August 2020 (Global Volcanism Program, 2020).

Analysis of volcanoes such as Nishinoshima is challenging, given its remote location. Remote sensing provides a way to monitor the different volcanic phenomena that occur during an eruptive cycle provided the temporal frequency is adequate. For example, Nishinoshima has

been analyzed using both unmanned aerial vehicles (UAVs; Ohminato et al., 2016) and satellite sensor platforms (e.g., Kaneko et al., 2019). Data from various satellite sensors have been used to derive information on the eruptive activity of Nishinoshima such as the morphology of lava flows (Maeno et al., 2016; Kaneko et al., 2019) and thermal anomalies (Kaneko et al., 2018, 2019).

Monitoring of volcanic ash emissions from space is routinely performed by high-temporal, low spatial resolution sensors, including those found on geostationary platforms, such as the Advanced Baseline Imager (ABI) on board the Geostationary Operational Environmental Satellite (GOES; e.g. Pavlonis et al., 2013) and the Spin Enhanced Visible and Infrared Imager (SEVIRI; e.g. Prata and Kerkmann, 2007). Polar orbiting satellites, such as the Moderate Resolution Imaging Spectroradiometer (MODIS; e.g. Watson et al., 2004) and the Infrared Atmospheric Sounding Interferometer (IASI; e.g. Klüser et al., 2013), provide less frequent coverage but are still very useful because of their improved spatial and spectral resolutions. Volcanic ash is discriminated from meteorological cloud primarily using the “split-window” technique to detect the differential absorption of ash relative to that of water vapor in two wavelength bands between 11 and 12 μm (Prata, 1989a, 1989b). This method requires upwelling ground radiance to pass through the cloud and be detected by the sensor, resulting in a Brightness Temperature (BT) difference upon comparison of the two bands. Volcanic ash clouds return negative values, whereas meteorological cloud returns positive values for most cases. This method has been further developed to provide information on the

* Corresponding author.

E-mail address: dbwilliams@pitt.edu (D.B. Williams).

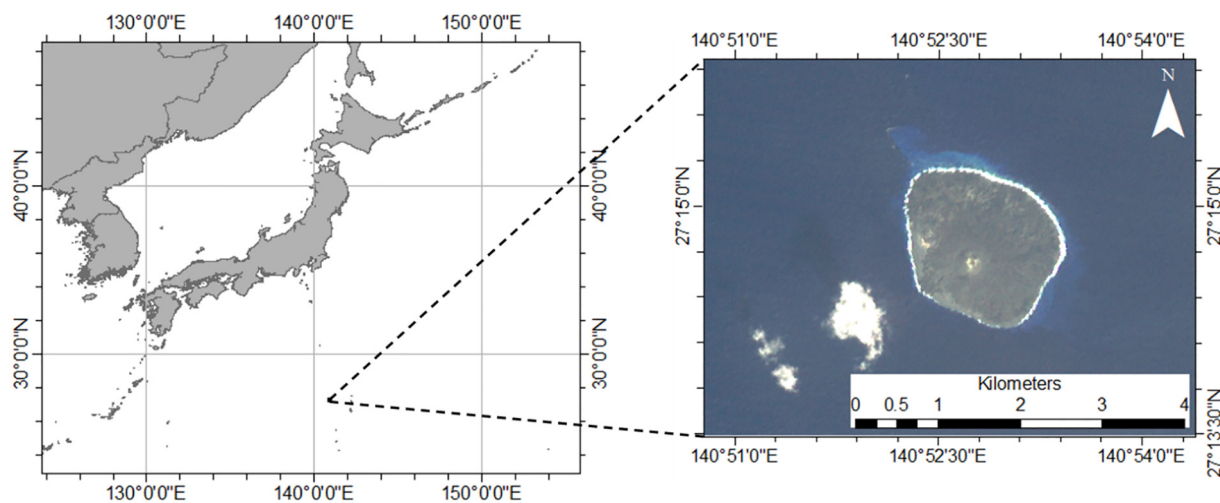


Fig. 1. Location of Nishinoshima volcano. The image on the right was collected by the ASTER sensor on 26 February 2017 before the island's shape changed dramatically following subsequent volcanic activity. ASTER VNIR Band 3, 2, 1 in R, G, B, respectively, with a spatial resolution of 15 m/pixel.

particle size distribution (PSD), plume altitude, mass loading, effective particle radius, and aerosol optical depth (AOD), using a combination of 2 or 3 bands to determine these properties (Wen and Rose, 1994; Prata and Grant, 2001; Pergola et al., 2004; Pavolonis et al., 2006; Lee et al., 2014; Guéhenneux et al., 2015; Merucci et al., 2016).

There are however well described errors with utilizing these methods (Simpson et al., 2000; Prata et al., 2001). These include the inability to directly measure plumes that are optically opaque to upwelling radiation, and detect those particles $>15\ \mu\text{m}$, as well as the need to assume the composition of ash to input optical properties into the model, which if incorrect, leads to inaccurate retrievals (Mackie et al., 2014). Furthermore, the current suite of sensors have spatial resolutions of $>1\ \text{km}^2$ in the TIR, meaning that smaller volcanic eruptions commonly go unnoticed or unanalyzed. However, work by Williams and Ramsey (2019) demonstrate the use of ASTER TIR data to extract both composition and particle size from the optically-thick plume bearing pixels proximal to the vent. They determine this optically-thick region of the plume using those pixels with low plume temperatures compared to the surface temperature. In the Williams and Ramsey (2019) model, the upper plume surface is treated as a solid emitting surface and the spectra from each pixel are linearly deconvolved using specific spectral library of ash samples (dubbed the ASTER Volcanic Ash Library, AVAL) to determine both the composition and the particle size.

In this paper we report initial findings on ash cloud composition and particle size generated from Nishinoshima during eruptive activity in July 2020 using ASTER TIR data. Nine scenes were acquired on five different dates by the ASTER sensor as part of the Urgent Request Protocol (URP) sensor-web (Ramsey, 2016; Ramsey and Flynn, 2020), from 8 to 31 July 2020. The TIR emissivity data were modeled using linear spectral deconvolution and the AVAL library (Ramsey and Christensen, 1998; Williams and Ramsey, 2019).

2. Materials and methods

2.1. ASTER data

The ASTER instrument on the Terra satellite has acquired $\sim 320,000$ scenes of volcanoes worldwide (Ramsey and Flynn, 2020). The sensor contains visible near infrared (VNIR) and TIR subsystems, at 15 and 90 m spatial resolution, respectively (Yamaguchi et al., 1998). Additionally, the sensor can point off nadir at a target (up to 8.55° for TIR; Pieri and Abrams, 2004). The combination of these capabilities led to the development of the ASTER URP (Duda et al., 2009; Ramsey, 2016; Ramsey and Flynn, 2020). The URP is triggered by thermal anomaly detections

using operational monitoring systems developed for MODIS such as MODVOLC (Wright et al., 2004) and MIROVA (Coppola et al., 2016). The initial thermal detections at Nishinoshima by MODVOLC triggered the URP system resulting in improved data acquisitions that included the three used in this study (Table 1).

There are various ASTER data products, representing different processing levels. This study used the level 2 emissivity product (AST_05), which is derived from AST_09T data, which is both atmospherically and radiometrically corrected (Abrams, 2000). The data are processed through the Temperature Emissivity Separation (TES) algorithm (Gillespie et al., 1998; Gustafson et al., 2006) to derive the per-pixel emissivity for the entire scene of an AST_05 product. These data are considered accurate to 0.015 emissivity units and used previously for similar deconvolution modeling (Williams and Ramsey, 2019).

2.2. The ASTER volcanic ash library

The retrieval of ash properties from orbital TIR data using emission spectroscopy relies on the availability of an appropriate spectral library. There are several different libraries available that contain infrared spectra of pure mineral samples, measured in both reflectance (e.g. Baldridge et al., 2009) and emissivity (e.g. Christensen et al., 2000). However, given that volcanic ash plumes contain a significant glass component (20–80%) coupled with multiple mineral phases (Horwell, 2007), existing libraries are not appropriate. Ash samples from 4 volcanoes were first used to create AVAL, along with a crushed sample of Mono-Inyo Domes obsidian, used as a proxy for high SiO_2 glass (Williams and Ramsey, 2019). This library continues to expand to include a wider

Table 1

ASTER data acquired of ash plumes from Nishinoshima over July 2020. Those highlighted in **bold** were used for this study. Images obtained in succession were mosaicked to capture the full extent of the plume. Two images were not used (19 and 28 July) owing to a processing error in the ASTER level 2 product generation that resulted in null emissivity values in a significant number of plume pixels.

Date	Time (UTC)	Granule ID
8/7/2020	12:45	AST_05.003:2386110004
	12:46	AST_05.003:2386109991
	01:29	AST_05.003:2389054772
19/7/2020	12:45	AST_05.003:2389812394
	12:46	AST_05.003:2389812443
28/7/2020	01:23	AST_05.003:2390670606
	12:51	AST_05.003:2391697176
	12:51	AST_05.003:2391697181
31/7/2020	12:52	AST_05.003:2391697154

range of compositions. The sample library will be made available in the archives of the University of Pittsburgh Image Visualizations and Infrared Spectroscopy research group website (<http://ivis.eps.pitt.edu/archives/>). Each sample is measured in the laboratory for different particle size ranges to account for the non-linearity of spectral mixing at particle sizes $<63 \mu\text{m}$ (Ramsey and Christensen, 1998). TIR emissivity spectra are obtained using a Nicolet Nexus 670 FTIR Spectrometer, using a cooled MCT-B detector, following the two-temperature method outlined by Ruff et al. (1997). Ash size fractions are placed in copper sample cups and heated to 80°C overnight. The cup is placed on a heated stage, which is in a purged glovebox adjacent to the FTIR spectrometer, to maintain the thermal equilibrium of the sample. The sample is raised into a temperature-controlled enclosure, kept at a constant 25°C , and the spectrum acquired. These steps are taken to remove unwanted atmospheric effects caused by H_2O and CO_2 . Each sample is scanned 512 times, which are subsequently averaged to improve the signal to noise (SNR) ratio, at a spectral sampling resolution of 4 cm^{-1} . The hyperspectral laboratory data are down-sampled to five-point spectral resolution using the ASTER TIR filter functions (Fig. 2).

2.3. Linear deconvolution model

The ASTER data are processed using the AVAL spectra and the linear deconvolution model of Ramsey and Christensen (1998). Because of the low plume opacity in thick ash plumes, no ground upwelling radiance is present, and the only source of radiant emission is the plume's upper surface. This emission mixes linearly as a function of the end member's areal abundance. The linear deconvolution model is based on the principle that each component contributes in areal proportionality to the overall spectrum. This can be expressed mathematically for η isothermal end members as,

$$\varepsilon(\lambda)_{\text{mix}} = \sum_{i=1}^{\eta} \zeta_i \varepsilon(\lambda)_i + \delta(\lambda); \sum_{i=1}^{\eta} \zeta_i = 1.0 \quad (1)$$

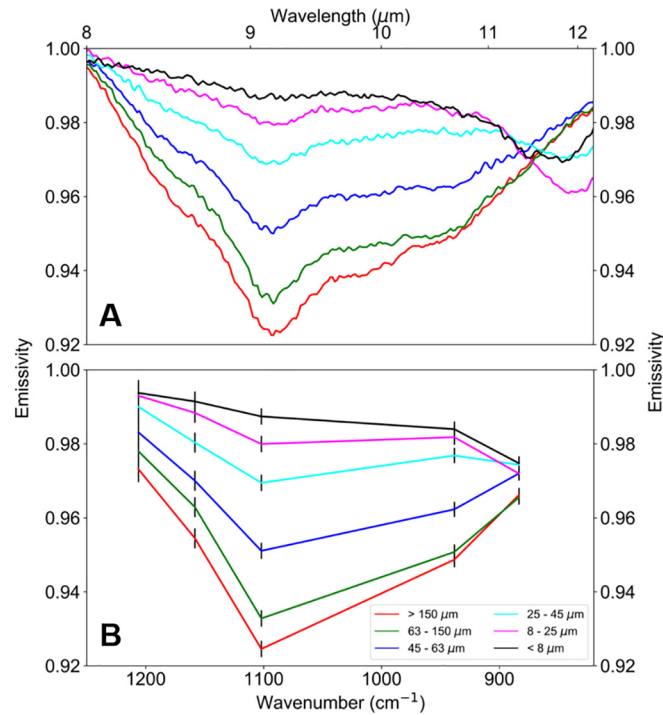


Fig. 2. AVAL data of Sakurajima (Japan) volcanic ash collected in 2013. [A] hyperspectral laboratory resolution, [B] laboratory data resampled to the ASTER TIR resolution. Each ash sample in the library contains six particle size fractions.

where $\varepsilon(\lambda)_{\text{mix}}$ is the mixture spectrum, ζ_i is the areal fraction of the i^{th} end member ($\varepsilon(\lambda)_i$), and $\delta(\lambda)$ is the per-band residual error. The model fit accuracy is given by the root-mean-square (RMS) error, which is a function of the residual error terms,

$$\text{RMS} = \sqrt{\sum_{j=1}^m \delta(\lambda)_j^2 / m} \quad (2)$$

where m is the number of instrument bands. Lower RMS values correspond to a better model fit. Applied to ASTER data, the model calculates the per-pixel percentage of each end member plus the RMS, which is useful in determining the spatial variation in the model fit.

To extract only the opaque plume pixels from the image, a more rigorous approach is employed than the temperature threshold used in Williams and Ramsey (2019). The optical depth of the plume is calculated, using ASTER radiance data from band 13 ($10.657 \mu\text{m}$), as this channel is sensitive to ash coupled with high atmospheric transmissivity. The method used is that of Garnier et al. (2012, 2015), which was adapted for use with the Atmospheric Infrared Sounder (AIRS) by Prata (2016) for the extraction of optical depth from ash plumes. Optical depth (τ_{IR}) is calculated using the following equation,

$$\tau_{\text{IR}} = -\ln \left[1 - \frac{R_s - R_m}{R_s - B_a} \right] \quad (3)$$

where R_s is the radiance at the surface, R_m is the per-pixel radiance, and B_a is the Planck radiance of the plume, which is controlled by the temperature of the plume height. The heights of each of the plumes was given by the Tokyo Volcano Ash Advisory Center (VAAC; <https://ds.data.jma.go.jp/svd/vaac/data/index.html>), with the plume temperature then derived from local radiosonde data (<http://weather.uwyo.edu/upperair/sounding.html>). The threshold used to determine opacity was $\tau_{\text{IR}} \geq 4$, which is reported in the literature (i.e., Rose et al., 1995, 2001; Schneider et al., 1999). This conservative value was used to mask the data, so only those pixels that were considered opaque were used in the deconvolution analysis. Some pixels returned null values using this method, owing to lower pixel temperatures than the temperature of the plume top height. These were mainly found in the portion of the plume closest to the vent, and were however included in the analysis, given that this region should in theory have the highest opacity.

3. Results

Analysis presented here focuses on three Nishinoshima plumes captured by ASTER on 8, 24 and 31 July 2020 (Figs. 3–5).

The size of the plumes varied from $\sim 15 \text{ km}$ long on 24 July 2020 (Fig. 4), to larger plumes on 8 (Fig. 3) and 31 July (Fig. 5), which both extend $\sim 75 \text{ km}$. However, only the first 20 km of the 31 July plume were modeled because of the conservative optical depth threshold, therefore many plume bearing pixels were discarded for the analysis. Where viewing conditions allowed, thermally elevated regions were also observed on the flanks of Nishinoshima, most likely representing lava flow activity (Global Volcanism Program, 2020). In each of the three cases presented, two AVAL sample suites provided the best model fit to the plume data. These are both andesite (58.46 to 60.16 wt% SiO_2) ash samples from Santiaguito volcano, Guatemala, and Sakurajima volcano, Japan. Andesite compositions have been previously measured from recent Nishinoshima samples (Tamura et al., 2019). Modeling the data with these end members returned the lowest RMS errors for each of the three dates. The difference in RMS between the retrievals using the two andesite spectral end members is typically within 0.1 in the region of the plume where the model returns an RMS of <0.5 . Therefore, the Santiaguito end member was chosen for the analysis presented here.

The model results produce composition as well as the best particle size range (displayed as a per pixel percentage of each ash end member).

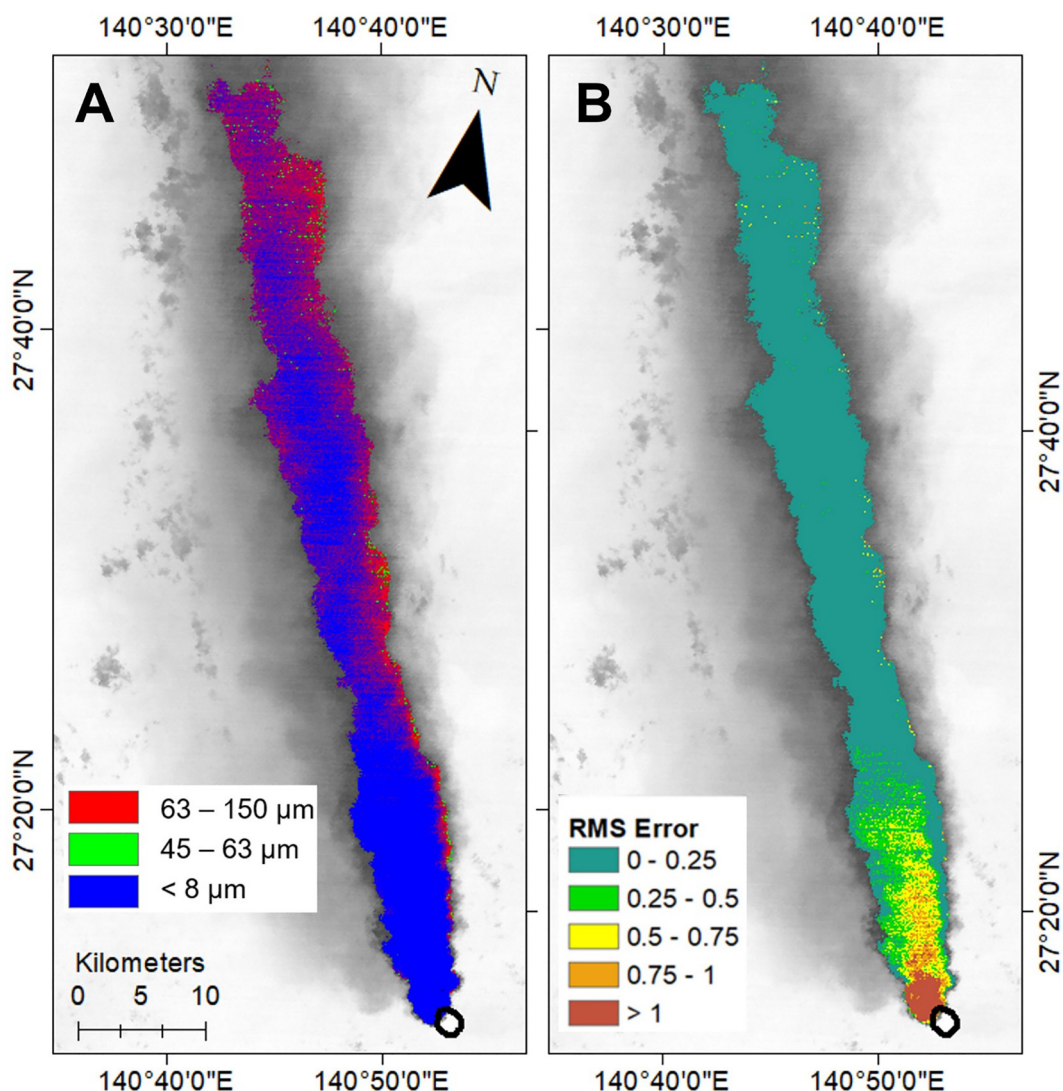


Fig. 3. Linear deconvolution results for the ASTER images acquired on 8 July 2020. The data were unmixed using the Santiaguito andesite end-member. [A] The three most dominant particle sizes. [B] The per-pixel RMS error result.

The three most abundant particle size ranges found for each image were 63–150 μm , 45–63 μm and <8 μm , which was consistent for both AVAL andesite samples. Overall, the <8 μm size range is detected closest to the vent and appears to make up the core of the plume's upper surface, becoming less prevalent towards the edges and distally from the vent. These regions have more of the 63–150 μm and 45–63 μm size fractions detected. The highest RMS values are associated with the region of the plume close to the vent and improved markedly in the downwind portion. The distribution of the particle sizes changes with plume size, with the larger plumes on 8 and 31 July having more fine-grained (<8 μm) particles compared to the smaller eruption observed on 24 July.

4. Discussion

The model results produce a best-fit to andesite, with no major variations over the course of the eruption. The wt% SiO_2 of the two AVAL andesite samples are consistent with the findings of Tamura et al. (2019). They reported on the geochemistry of more recently erupted Nishinoshima andesites, which have an SiO_2 content of ~60%. The good spectral fit of AVAL andesite end members is therefore encouraging and consistent with the model behavior. Because of this, the Santiaguito end member was selected for the analysis of all the images.

The RMS image results show the regions where the library spectra are a good model fit to the image spectra, as well as those areas where the fit is poor. One point of interest is the high RMS errors seen consistently over the summit of the volcano and in the first several kilometers of the drifting cloud. The RMS then subsequently decreases to values <0.1. The exact cause of this poor fit is likely a combination of factors, which need to be explored further. Most likely is the higher amount of water vapor and water ice at higher altitudes entrained in the plume, which affects the TIR spectral shape (Gangale et al., 2010). Excess water vapor not removed by the standard ASTER atmospheric correction most affects the shortest wavelength TIR band (band 10) and ice affects the longest wavelengths (bands 13 and 14). Both effects are seen in the proximal regions of the plume with the highest RMS errors. Future work is exploring the incorporation of an ice spectrum into the AVAL library.

The particle size variations are also similar between images, with a core of finer particles that dominate the proximal regions and the center of the plume. The quantity of fine to coarse particles appears to be affected by the size of the plume, with the larger eruptions having a more regions of their plumes dominated by the <8 μm end-member. The 8 July 2020 plume contains the largest amount of this size fraction. These distributions are the result of either more fragmentation occurring in the larger eruptions, or a function of the actual plume "surface"

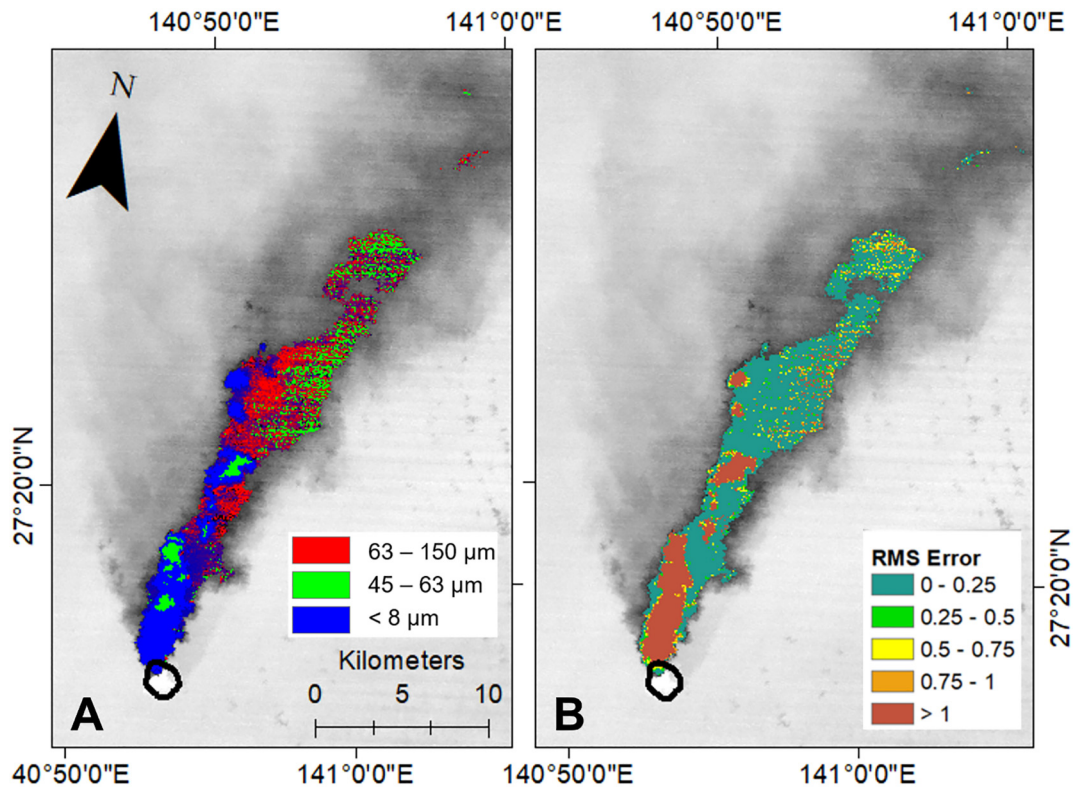


Fig. 4. Linear deconvolution results for the ASTER images acquired on 24 July 2020. The data were unmixed using the Santiaguito andesite end-member. [A] The three most dominant particle sizes. [B] The per-pixel RMS error result.

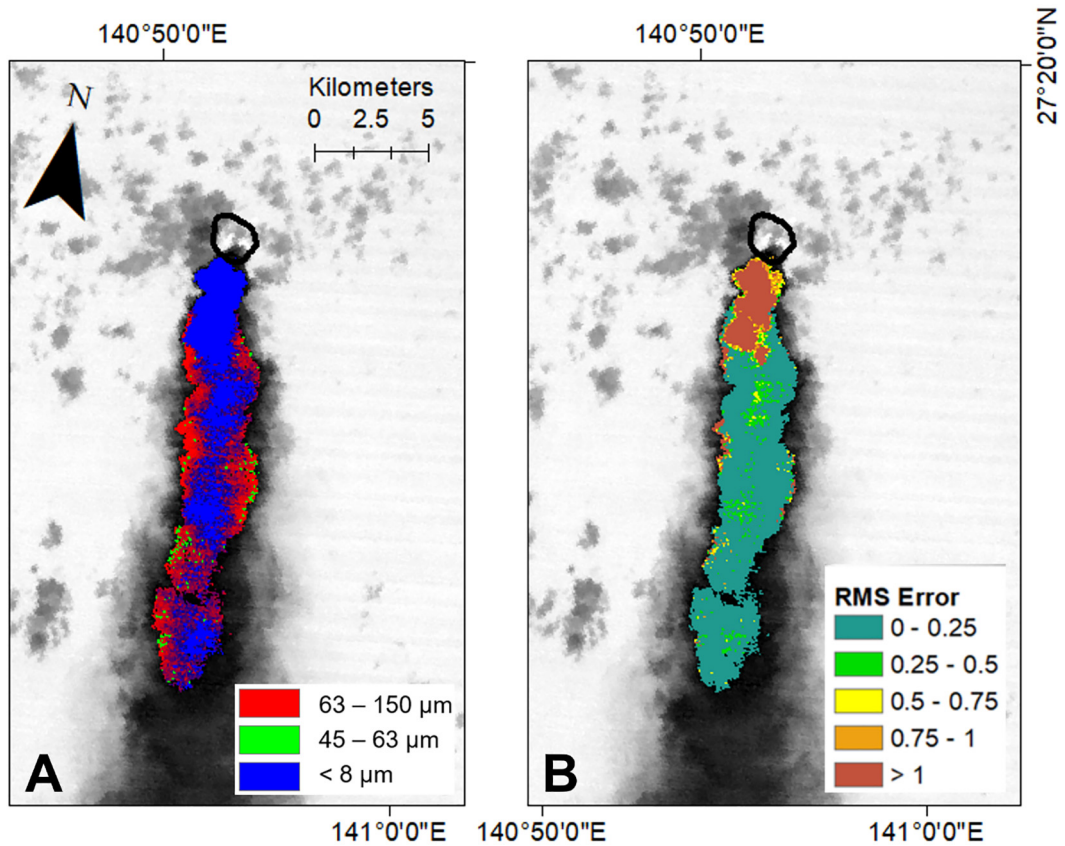


Fig. 5. Linear deconvolution results for the ASTER images acquired on 31 July 2020. The data were unmixed using the Santiaguito andesite end-member. [A] The three most dominant particle sizes. [B] The per-pixel RMS error result.

being detected and modeled. As the plume drifts away from the volcano and begins to stratify, it becomes more transparent at the top. Larger particles settle through the atmosphere faster than finer particles, therefore, emitted energy from these ash layers deeper in the plume containing coarser particles is preferentially sampled. This change with time and distance in essence allows different depths within the plume to be probed, sensing those larger particles that are settling towards the lower portion of the plume. This effect leads to the apparent bi-modality of the plumes observed. The deeper layers further from the vent, where larger particles (63–150 μm particle size) are present, act as the solid emitting surface. Layers above are much more diffuse, allowing this layer to be preferentially sampled. Some of the pixels towards the edge of the plume, where the 45–63 μm dominates (most evident in the 24 July 2020 image; Fig. 4), are also associated with higher RMS errors. Here, this end member has been selected by the model as the best fit. These pixels are commonly associated with emissivity values greater than 1 in ASTER Band 10 due to water vapor, which contributes to this poor model fit. Additionally, these higher RMS errors may also be as a result of scan line noise which results in apparent striping of the ASTER emissivity data. Where optical depth decreases to <4 , upwelling radiance from the surface and underlying atmosphere is transmitted through the plume and reach the sensor, creating a more complex mixed signal which was not analyzed as part of this study.

5. Conclusions

This study provides a quantitative spectral analysis of three ash plumes generated by Nishinoshima volcano during July 2020. It is the first time that this ash plume modeling approach has been used operationally in conjunction with the ASTER URP program. The number of successful acquisitions by the ASTER sensor shows the efficacy of this sensor-web, and with the AVAL-based modeling, allows the simultaneous retrievals of both composition and particle size at high spatial resolution. The best model fit was an andesite composition consistently throughout the eruption duration (based on the low RMS errors), which indicates no compositional transitions with time. Model-based particle size ranges were also consistent in pattern for each of the plumes, with the larger eruptions and larger plumes having higher amounts of the smallest size fraction. With distance from the vent and particle size stratification in the plume, larger particle size fractions were retrieved more consistently.

The ASTER sensor is shown to be sensitive to volcanic plumes at a variety of scales and can observe small- and large-scale emissions. Furthermore, this method of extracting the composition of volcanic ash better informs transmission spectroscopic retrievals of volcanic ash, leading to a greater accuracy using these methods (Mackie et al., 2014). Additionally, this method is applicable to other current and future TIR sensors, provided the plume has an opaque portion, the pixel scale is small enough relative to the plume size, and the spectral resolution is sufficient to resolve features. The AVAL library is continually expanding, with additional compositional suites being added to improve the model's dynamic range and more accurately retrieve composition and particle size from future plume-forming eruptions.

Declaration of Competing Interest

The authors declare that they have no known competing financial interests or personal relationships that could have appeared to influence the work reported in this paper.

Acknowledgments

We would like to thank the editor, Dr. Diana Roman, and the comments of two anonymous reviewers which greatly improved this manuscript. We would also like to thank Drs Andrew Prata and Vince Realmuto for their advice on this work. Funding for this work is

provided by a NASA Science of Terra, Aqua, and Suomi NPP grant (80NSSC18K1001) awarded to MSR.

References

- Abrams, M., 2000. The Advanced Spaceborne Thermal Emission and Reflection Radiometer (ASTER): data products for the high spatial resolution imager on NASA's Terra platform. *International. J. Remote Sens.* 21 (5), 847–859. <https://doi.org/10.1080/014311600210326>.
- Baldrige, A.M., Hook, S.J., Grove, C.I., Rivera, G., 2009. The ASTER spectral library version 2.0. *Remote Sens. Environ.* 113 (4), 711–715. <https://doi.org/10.1016/j.rse.2008.11.007>.
- Christensen, P.R., Bandfield, J.L., Hamilton, V.E., Howard, D.A., Lane, M.D., Piatek, J.L., Ruff, S.W., Stefanov, W.L., 2000. A thermal emission spectral library of rock-forming minerals. *J. Geophys. Res. Planets* 105 (E4), 9735–9739. <https://doi.org/10.1029/1998JE000624>.
- Coppola, D., Laiolo, M., Cigolini, C., Donne, D.D., Ripepe, M., 2016. Enhanced volcanic hot-spot detection using MODIS IR data: results from the MIROVA system. *Geol. Soc. Lond. Spec. Publ.* 426, 181–205. <https://doi.org/10.1144/SP426.5>.
- Duda, K.A., Ramsey, M., Wessels, R., Dehn, J., Ho, P.P., 2009. *Optical satellite volcano monitoring: a multi-sensor rapid response system*. *Geosci. Remote Sens.* 473–496.
- Gangale, G., Prata, A.J., Clarisse, L., 2010. The infrared spectral signature of volcanic ash determined from high-spectral resolution satellite measurements. *Remote Sens. Environ.* 114 (2), 414–425. <https://doi.org/10.1016/j.rse.2009.09.007>.
- Garnier, A., Pelon, J., Dubuisson, P., Faivre, M., Chomette, O., Pascal, N., Kratz, D.P., 2012. Retrieval of cloud properties using CALIPSO Imaging infrared Radiometer. Part I: effective emissivity and optical depth. *J. Appl. Meteorol. Climatol.* 51 (7), 1407–1425. <https://doi.org/10.1175/JAMC-D-11-0220.1>.
- Garnier, A., Pelon, J., Vaughan, M.A., Winker, D.M., Trepte, C.R., Dubuisson, P., 2015. Lidar multiple scattering factors inferred from CALIPSO lidar and IIR retrievals of semi-transparent cirrus cloud optical depths over oceans. *Atmos. Measurement Techniques* 8 (7), 2759–2774. <https://doi.org/10.5194/amt-8-2759-2015>.
- Gillespie, A., Rokugawa, S., Matsunaga, T., Cothorn, J.S., Hook, S., Kahle, A.B., 1998. A temperature and emissivity separation algorithm for Advanced Spaceborne thermal Emission and Reflection Radiometer (ASTER) images. *IEEE Trans. Geosci. Remote Sens.* 36 (4), 1113–1126. <https://doi.org/10.1109/36.700995>.
- Global Volcanism Program, 2020. Report on Nishinoshima (Japan). In: Craddock, A.E., Venzke, E. (Eds.), *Bulletin of the Global Volcanism Network*. 45(9). Smithsonian Institution. <https://doi.org/10.5479/si.GVP.BGVN202009-284096>.
- Guéhenneux, Y., Gouhier, M., Labazuy, P., 2015. Improved space borne detection of volcanic ash for real-time monitoring using 3-Band method. *J. Volcanol. Geotherm. Res.* 293, 25–45. <https://doi.org/10.1016/j.jvolgeores.2015.01.005>.
- Gustafson, W.T., Gillespie, A.R., Yamada, G.J., 2006. Revisions to the ASTER temperature/emissivity separation algorithm. 2nd International Symposium on Recent Advances in Quantitative Remote Sensing, Torrent (Valencia), Spain.
- Horwell, C.J., 2007. Grain-size analysis of volcanic ash for the rapid assessment of respiratory health hazard. *J. Environ. Monit.* 9 (10), 1107–1115. <https://doi.org/10.1039/B710583P>.
- Kaneko, T., Yasuda, A., Yoshizaki, Y., Takasaki, K., Honda, Y., 2018. Pseudo-thermal anomalies in the shortwave infrared bands of the Himawari-8 AHI and their correction for volcano thermal observation. *Earth Planets Space* 70 (1), 175. <https://doi.org/10.1186/s40623-018-0956-8>.
- Kaneko, T., Maeno, F., Yasuda, A., Takeo, M., Takasaki, K., 2019. The 2017 Nishinoshima eruption: combined analysis using Himawari-8 and multiple high-resolution satellite images. *Earth Planets Space* 71 (1), 1–18. <https://doi.org/10.1186/s40623-019-1121-8>.
- Klüser, L., Erbertseder, T., Meyer-Arneck, J., 2013. Observation of volcanic ash from Puyehue-Cordón Caulle with IASI. *Atmos. Measurement Techniques* 6 (1), 35. <https://doi.org/10.5194/amt-6-35-2013>.
- Lee, K.H., Wong, M.S., Chung, S.R., Sohn, E., 2014. Improved volcanic ash detection based on a hybrid reverse absorption technique. *Atmos. Res.* 143, 31–42. <https://doi.org/10.1016/j.atmosres.2014.01.019>.
- Mackie, S., Millington, S., Watson, I.M., 2014. How assumed composition affects the interpretation of satellite observations of volcanic ash. *Meteorol. Appl.* 21 (1), 20–29. <https://doi.org/10.1002/met.1445>.
- Maeno, F., Nakada, S., Kaneko, T., 2016. Morphological evolution of a new volcanic islet sustained by compound lava flows. *Geology* 44 (4), 259–262. <https://doi.org/10.1130/G37461.1>.
- Merucci, L., Zakšek, K., Carboni, E., Corradini, S., 2016. Stereoscopic estimation of volcanic ash cloud-top height from two geostationary satellites. *Remote Sens.* 8 (3), 206. <https://doi.org/10.3390/rs8030206>.
- Ohminato, T., Kaneko, T., Takagi, A., 2016. UAV observation of newly formed volcanic island, Nishinoshima, Japan, from a ship. AGUFM, 2016, NH13B-04.
- Osaka, J., Ohira, Y., Minato, I., 1974. On the submarine eruption of Nishinoshima. *Bull. Volcanol. Soc. Jpn 2nd Ser.* 18 (3), 173–174.
- Pavlonis, M.J., Feltz, W.F., Heidinger, A.K., Gallina, G.M., 2006. A daytime complement to the reverse absorption technique for improved automated detection of volcanic ash. *J. Atmos. Ocean. Technol.* 23 (11), 1422–1444. <https://doi.org/10.1175/JTECH1926.1>.
- Pavlonis, M.J., Heidinger, A.K., Sieglaff, J., 2013. Automated retrievals of volcanic ash and dust cloud properties from upwelling infrared measurements. *J. Geophys. Res.-Atmos.* 118 (3), 1436–1458.
- Pergola, N., Tramutoli, V., Marchese, F., Scaffidi, I., Lacava, T., 2004. Improving volcanic ash cloud detection by a robust satellite technique. *Remote Sens. Environ.* 90 (1), 1–22. <https://doi.org/10.1016/j.rse.2003.11.014>.

- Pieri, D., Abrams, M., 2004. ASTER watches the world's volcanoes: a new paradigm for volcanological observations from orbit. *J. Volcanol. Geotherm. Res.* 135 (1–2), 13–28. <https://doi.org/10.1016/j.jvolgeores.2003.12.018>.
- Prata, A.J., 1989a. Observations of volcanic ash clouds in the 10–12 μm window using AVHRR/2 data. *Int. J. Remote Sens.* 10 (4–5), 751–761. <https://doi.org/10.1080/01431168908903916>.
- Prata, A.J., 1989b. Infrared radiative transfer calculations for volcanic ash clouds. *Geophys. Res. Lett.* 16 (11), 1293–1296. <https://doi.org/10.1029/GL016i011p01293>.
- Prata, A.T., 2016. *Active and Passive Satellite Remote Sensing of Volcanic Clouds* Doctoral Dissertation. Monash University, Melbourne, Australia.
- Prata, A.J., Grant, I.F., 2001. Retrieval of microphysical and morphological properties of volcanic ash plumes from satellite data: Application to Mt Ruapehu, New Zealand. *Q. J. R. Meteorol. Soc.* 127 (576), 2153–2179. <https://doi.org/10.1002/qj.49712757615>.
- Prata, A.J., Kerkmann, J., 2007. Simultaneous retrieval of volcanic ash and SO₂ using MSG-SEVIRI measurements. *Geophys. Res. Lett.* 34 (5). <https://doi.org/10.1029/2006GL028691>.
- Prata, F., Bluth, G., Rose, B., Schneider, D., Tupper, A., 2001. Comments on “failures in detecting volcanic ash from a satellite-based technique”. *Remote Sens. Environ.* 78 (3), 341–346. [https://doi.org/10.1016/S0034-4257\(01\)00231-0](https://doi.org/10.1016/S0034-4257(01)00231-0).
- Ramsey, M.S., 2016. Synergistic use of satellite thermal detection and science: a decadal perspective using ASTER. *Geol. Soc. Lond., Spec. Publ.* 426 (1), 115–136. <https://doi.org/10.1144/SP426.23>.
- Ramsey, M.S., Christensen, P.R., 1998. Mineral abundance determination: Quantitative deconvolution of thermal emission spectra. *J. Geophys. Res. Solid Earth* 103 (B1), 577–596. <https://doi.org/10.1029/97JB02784>.
- Ramsey, M.S., Flynn, I.T., 2020. The spatial and spectral resolution of ASTER infrared image data: a paradigm shift in volcanological remote sensing. *Remote Sens.* 12 (4), 738. <https://doi.org/10.3390/rs12040738>.
- Rose, W.I., Delene, D.J., Schneider, D.J., Bluth, G.J.S., Krueger, A.J., Sprod, I., ... Ernst, G.G., 1995. Ice in the 1994 Rabaul eruption cloud: implications for volcano hazard and atmospheric effects. *Nature* 375 (6531), 477–479. <https://doi.org/10.1038/375477a0>.
- Rose, W.I., Bluth, G.J., Schneider, D.J., Ernst, G.G., Riley, C.M., Henderson, L.J., McGimsey, R.G., 2001. Observations of volcanic clouds in their first few days of atmospheric residence: the 1992 eruptions of Crater Peak, Mount Spurr Volcano, Alaska. *J. Geol.* 109 (6), 677–694. <https://doi.org/10.1086/323189>.
- Ruff, S.W., Christensen, P.R., Barbera, P.W., Anderson, D.L., 1997. Quantitative thermal emission spectroscopy of minerals: a laboratory technique for measurement and calibration. *J. Geophys. Res. Solid Earth* 102 (B7), 14899–14913. <https://doi.org/10.1029/97JB00593>.
- Schneider, D.J., Rose, W.I., Coke, L.R., Bluth, G.J., Sprod, I.E., Krueger, A.J., 1999. Early evolution of a stratospheric volcanic eruption cloud as observed with TOMS and AVHRR. *J. Geophys. Res.-Atmos.* 104 (D4), 4037–4050. <https://doi.org/10.1029/1998JD200073>.
- Simpson, J.J., Hufford, G., Pieri, D., Berg, J., 2000. Failures in detecting volcanic ash from a satellite-based technique. *Remote Sens. Environ.* 72 (2), 191–217. [https://doi.org/10.1016/S0034-4257\(99\)00103-0](https://doi.org/10.1016/S0034-4257(99)00103-0).
- Špičák, A., Vaněk, J., Hanuš, V., 2009. Seismically active column and volcanic plumbing system beneath the island arc of the Izu-Bonin subduction zone. *Geophys. J. Int.* 179 (3), 1301–1312. <https://doi.org/10.1111/j.1365-246X.2009.04375.x>.
- Tamura, Y., Ishizuka, O., Sato, T., Nichols, A.R., 2019. Nishinoshima volcano in the Ogasawara Arc: New continent from the ocean? *Island Arc* 28 (1), e12285. <https://doi.org/10.1111/iar.12285>.
- Watson, I.M., Realmuto, V.J., Rose, W.I., Prata, A.J., Bluth, G.J., Gu, Y., Bader, C.E., Yu, T., 2004. Thermal infrared remote sensing of volcanic emissions using the moderate resolution imaging spectroradiometer. *J. Volcanol. Geotherm. Res.* 135 (1–2), 75–89. <https://doi.org/10.1016/j.jvolgeores.2003.12.017>.
- Wen, S., Rose, W.I., 1994. Retrieval of sizes and total masses of particles in volcanic clouds using AVHRR bands 4 and 5. *J. Geophys. Res.-Atmos.* 99 (D3), 5421–5431. <https://doi.org/10.1029/93JD03340>.
- Williams, D.B., Ramsey, M.S., 2019. On the Applicability of Laboratory thermal infrared Emissivity Spectra for Deconvolving Satellite Data of Opaque Volcanic Ash Plumes. *Remote Sens.* 11 (19), 2318. <https://doi.org/10.3390/rs11192318>.
- Wright, R., Flynn, L.P., Garbeil, H., Harris, A.J., Pilger, E., 2004. MODVOLC: near-real-time thermal monitoring of global volcanism. *J. Volcanol. Geotherm. Res.* 135 (1–2), 29–49. <https://doi.org/10.1016/j.jvolgeores.2003.12.008>.
- Yamaguchi, Y., Kahle, A.B., Tsu, H., Kawakami, T., Pniel, M., 1998. Overview of advanced spaceborne thermal emission and reflection radiometer (ASTER). *IEEE Trans. Geosci. Remote Sens.* 36 (4), 1062–1071. <https://doi.org/10.1109/36.700991>.